PHYSICAL REVIEW B **95**, 081303(R) (2017)

Spin injection beyond the diffusive limit in the presence of spin-orbit coupling

Lennart-Knud Liefeith,[1,*] Rajkiran Tholapi,[1] Tomotsugu Ishikura,[2] Max Hänze,[1] Robert Hartmann,[1] Taras Slobodskyy,[1] and Wolfgang Hansen[1]

[1]*Institut für Nanostruktur- und Festkörperphysik, Universität Hamburg, 20355 Hamburg, Germany*
[2]*Research Center for Integrated Quantum Electronics (RCIQE), Hokkaido University, Sapporo 060-8628, Japan*

(Received 7 October 2016; revised manuscript received 19 December 2016; published 27 February 2017)

Spin injection from epitaxial iron into InGaAs/InAs quantum wells is observed using an all-electric nonlocal setup. From the choice of material, a significant spin-orbit interaction (SOI) is expected. The contact separation of the spin-valve devices is in the order of the mean free path so that the transport is at the transition between diffusive and ballistic. With an established purely diffusive model a spin-injection efficiency of 77% is determined from the data. This value is very large compared to previous observations on diffusive spin-valve devices on similar material systems. Motivated by similar results on ballistic spin-valve devices in a material system with small spin-orbit coupling, a recent model was suggested in which a ballistic spin-dephasing length was pointed out to be the crucial length scale. With this model and an experimentally determined spin-orbit coupling parameter of $\alpha = 4 \times 10^{-12}$ eV m, very high spin-injection efficiencies are still determined in our quantum wells. We suggest that the spin-dephasing length to be used in the model must be larger due to the crystallographic anisotropy of the spin-orbit coupling, i.e., in our setup the SOI stabilizes the spin in the crystal direction of the spin-polarized current.

DOI: 10.1103/PhysRevB.95.081303

Recently, spin injection in the ballistic limit has attracted attention [1,2] as, surprisingly, up to unphysically large spin-injection efficiencies have been derived with the standard diffusive model [2]. This points out an urgent need for a new theory modeling spin injection in the ballistic limit. A corresponding model was proposed by Chen *et al.* [3], in which a ballistic spin-dephasing length that exclusively depends on the spin-orbit coupling is set as a new key parameter. InAlAs heterostructures containing InGaAs/InAs quantum wells are known to combine the Rashba and Dresselhaus spin-orbit interaction (SOI) [4,5] with a large mean free path. Thus, InAlAs heterostructures are well suited for studies on spin injection in the ballistic limit under the influence of spin-obit coupling. Furthermore, spin-polarized currents in InGaAs/InAs quantum wells are suggested for device applications [6–8] rendering tunneling barriers redundant in the ballistic limit. So far only very few reports on all-electric spin injection in the InGaAs/InAs quantum wells exist [9–12]. In only one case the setup dimensions allow for ballistic transport [9]. However, due to the lack of a proper theoretical model, the quantitative determination of a spin-injection efficiency was not attempted in this work. In the reports on diffusive spin-valve devices [10–12], the calculated spin-injection efficiencies remain moderate, with a maximum value of 8% when a MgO tunneling barrier was inserted at the metal-semiconductor interface [12].

Fe/InAlAs heterostructures are grown in a connected multichamber molecular beam epitaxy cluster that allows for a high crystalline quality and contamination-free interfaces. The heterostructure layout is similar to previous reports [13–16], with a layer sequence as shown in Table I. The indium content, layer thicknesses, and crystalline quality have been verified *in situ* with reflection high electron energy diffraction and *ex situ* by using x-ray diffraction. In the following, the layer functionality is explained from top to bottom.

The topmost gold layer protects the subsequent iron layer that serves as the ferromagnetic spin polarizer. The following five semiconductor layers form an InGaAs quantum well (QW) embedded in undoped InAlAs barrier layers. The first layer, called the InAlAs cover layer, has a thickness of 10 nm. This value was optimized in previous investigations, in which it was found that the carrier mobility μ and carrier concentration N_s delicately depend on the InAlAs cover-layer thickness towards no electrical conduction without a cover layer. The chosen 10 nm is a compromise between low contact resistivity and inhibited carrier transport in the QW. The QW contains a 4 nm thin, pure InAs channel sandwiched between two $In_{0.74}Ga_{0.26}As$ layers. Different thicknesses are chosen for these layers to further enhance the structure inversion asymmetry in the channel. The InAlAs spacer layer separates the doping region from the QW. The doping layer contains a silicon doping concentration of 3×10^{18} cm^{-3}.

The corresponding conduction band profile and the electron density distribution calculated with the self-consistent Poisson and Schrödinger equation solver NEXTNANOMAT [17] are shown in Fig. 1(a). Importantly, the maximum of the carrier density n_s is located in the InAs channel and the first and second subbands are energetically located above the Fermi level E_f, indicating exclusive conduction by the ground state. In the calculation, the Schottky barrier height $\Phi_0 = 0.17$ eV has been adjusted so that the calculated carrier concentrations in the channel match the experimentally determined ones.

The transport properties in the QWs are determined from Shubnikov–de Haas oscillations and the Hall effect [18,19] from Hall bars at liquid helium temperatures. The Hall bars have a channel width of $w = 20$ μm and longitudinal contact spacings of 600 μm. They are oriented such that the current flows in the $[1\bar{1}0]$ direction. This direction matches the spin-current direction in the spin-valve devices. The Shubnikov–de Haas (SdH) oscillations in the longitudinal resistivity ρ_{xx} and the slope in the Hall resistivity ρ_{xy} are shown in Fig. 1(b). Clear signatures of a two-dimensional electron gas (2DEG)

---

[*] lliefeit@physnet.uni-hamburg.de

TABLE I. Layer sequence of the InAlAs heterostructure design. The bold region highlights the layers forming the QW.

Material	Function	Thickness (nm)
Au	Cap	7
Fe	Electrode	4
$In_{0.74}Al_{0.26}As$	Cover layer	10
$In_{0.74}Ga_{0.26}As$	**Subchannel**	**11**
InAs	**Channel**	**4**
$In_{0.74}Ga_{0.26}As$	**Subchannel**	**2**
$In_{0.74}Al_{0.26}As$	Spacer	10
$In_{0.74}Al_{0.26}As$	n^{++} doping	7
$In_{0.74}Al_{0.26}As$	Virtual substrate	530
	Buffer/superlattice	
	(001) GaAs	

are observed in both ρ_{xx} and the quantum Hall plateaus [20] of ρ_{xy}. From the magnetotransport measurements a carrier density $N_s = 4.8 \times 10^{11}$ cm^{-2} and a carrier mobility $\mu = 1 \times 10^5$ cm^2/V s are calculated, yielding a carrier mean free path $\lambda_{mfp} = \frac{\mu}{e}\hbar\sqrt{2\pi N_s}$ of 1.2 μm in the QWs. From the good agreement of the carrier densities calculated from the SdH oscillations $N_{s,SdH}$ and the Hall slope $N_{s,Hall}$, we exclude the existence of a secondary conducting channel.

Figure 1(c) shows the bias-dependent conductance G and differential conductance G_{diff} of the Au/Fe/InAlAs/QW injector electrode. The corresponding current I-V U_{3T} characteristics were recorded utilizing a three-terminal setup, where U_{3T} describes the voltage drop across the injector electrode. In our convention the reverse bias direction corresponds to carrier injection from the iron electrode into the QW and the forward bias direction to carrier subtraction from the QW. At zero bias a contact resistivity ρ_c of the injector electrode of 45×10^6 $\Omega\,\mu$m^2 is calculated.

In the extraction direction the conductance increases exponentially with the bias. In a first rough estimation of the tunneling current we employ the Simmons model [21] assuming a trapezoid-shaped tunneling barrier between two 3D electrodes. A fit to the shape of the current-voltage characteristics, which is shown in the inset of Fig. 1(c), yields an average tunneling-barrier height of $\Phi_{mean} = 100$ meV and an average tunnel-barrier width of $d = 15$ nm. In view of the simplicity of this approximation, we consider these values in good agreement with the calculated band profile. For negative U_{3T}, i.e., electron injection, G increases stepwise with the bias. We associate this stepwise increase with carrier tunneling from the 3D density of states (DOS) in iron into the first and second subbands of the 2DEG in the QW [22,23]. If we assign the inflection points in G_{diff} to the energetic positions of the higher subband edges in the QW, we obtain 80 and 200 meV

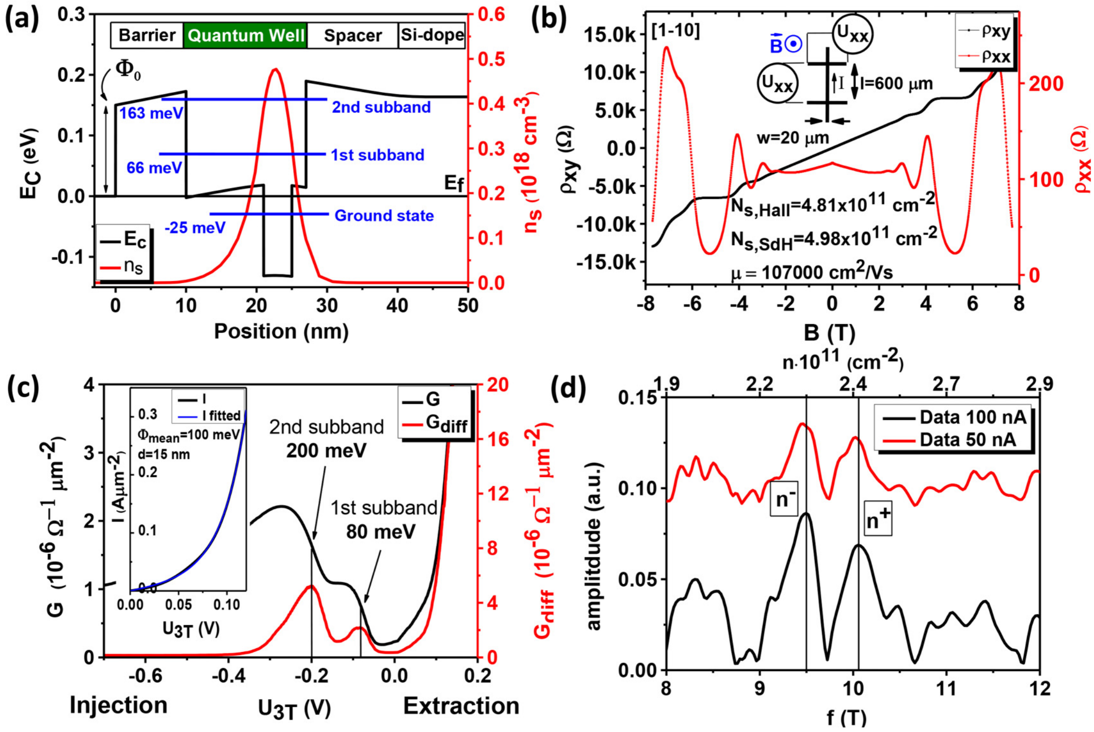

FIG. 1. (a) Conduction band E_c and three-dimensional carrier concentration n_s profiles of the InAlAs heterostructures in the growth direction. Electronic energies are quoted with respect to the Fermi energy E_f. The calculated ground, first, and second excited subband edges in the QW are indicated by blue horizontal lines. (b) Magnetotransport measurements on a standard Hall bar at liquid helium temperature. The inset sketches the setup. (c) Conductance G and differential conductance G_{diff} of the injector electrode No. 3. The inflection points assigned to the energetic positions of the first and second subbands in the QW are marked by vertical lines. The inset shows a fit with the Simmons model to the I-V characteristics in the forward bias direction. (d) Fourier transform of the longitudinal resistance ρ_{xx} vs $1/B$ in the regime $B < 3$ T for two sets of data taken at different currents I. The data were recorded separately at 250 mK. The peaks corresponding to spin-up n^+ and spin-down n^- densities are indicated.

for the onset of the first and second subband, respectively. These values are only 20% larger than the predictions of the above Poisson and Schrödinger solver calculations. We thus believe that the stepwise increase of the current in the injection direction directly reflects the quantized 2DEG of the QW.

The spin-orbit coupling parameter α is determined in separate magnetotransport measurements on Hall bars with reduced dimensions, i.e., a channel width of 2 μm and a longitudinal contact separation of 10 μm. The Hall bars are likewise oriented in the $[1\bar{1}0]$ crystal direction. The measurements were conducted at 250 mK in order to enhance SdH oscillations at small perpendicular magnetic fields. The corresponding magnetotransport data are not shown here. In the measurements, beating patterns are observed in ρ_{xx} vs $1/B$. The pattern is assigned to the SOI-induced energetic spin splitting in two subbands with populations n^+ and n^- [24–26]. The fast Fourier transforms (FFTs) of two linear interpolated data sets ρ_{xx} vs $1/B$ at different currents are shown in Fig. 1(d). We determine the densities $n^+ = 2.41 \times 10^{15}$ m^{-2} and $n^- = 2.30 \times 10^{15}$ m^{-2} from the peaks in the FFT. Their sum is close to the total carrier density determined from the Hall slope $N_{\mathrm{s,Hall}} = 4.8 \times 10^{11}$ cm^{-2}. From the beating pattern, α is calculated by [25]

$$\alpha = \frac{(n^+ - n^-)\hbar^2}{m^*}\sqrt{\frac{\pi}{2N_{\mathrm{s,Hall}} - 2(n^+ - n^-)}}, \qquad (1)$$

where $m^* = 0.036m_e$ is the effective mass [24],$\hbar$ is the Planck constant, and $n^\pm = \frac{e}{h} f(T)^\pm$. Equation (1) yields a spin-orbit coupling parameter of $\alpha = 4 \times 10^{-12}$ eV m in the quantum wells.

To assess the spin-injection efficiency we use lateral spin-valve devices in a nonlocal setup [27–30], which decouples the charge current and the measured spin potential. The spin-valve devices are fabricated using a combination of photo- and electron beam lithography and wet etching techniques. The lateral spin-valve device on which the following data were recorded is shown in Fig. 2(b). In total, four samples were prepared, from which only one was functional. It contains four iron electrodes (No. 2–No. 5) on a 25 μm wide mesa. The mesa is oriented in $[1\bar{1}0]$, defining the current direction in the quantum well. As indicated in Fig. 2(a), in the nonlocal setup the spin injection is measured with two separate circuits for current injection and voltage measurement [27–30]. The spin polarization is electrically injected via a current in an iron injector electrode and it is electrically detected by an iron detector electrode in close proximity to the injector. With the circuitry exemplarily depicted in Fig. 2(a), the injector is electrode No. 3 and the detector is electrode No. 2. The iron electrodes have different widths of either 2 μm (electrodes No. 2 and No. 4) or 3 μm (electrodes No. 3 and No. 5) and edge-to-edge spacings of 0.5 μm between electrodes No. 2 and No. 3, 2 μm between electrodes No. 3 and No. 4, and 1 μm between electrodes No. 4 and No. 5. The distance of the reference electrodes (No. 1 and No. 6) to the center iron electrodes is much larger with respect to the spin-relaxation length. In Fig. 2(c) the length of λ_{mfp} is compared to the extent and separation of the center electrodes. Since λ_{mfp} is larger than the edge-to-edge electrode separation but smaller than the center-to-center distance, the transport between the injector and the detector electrodes is believed to contain both diffusive and ballistic contributions.

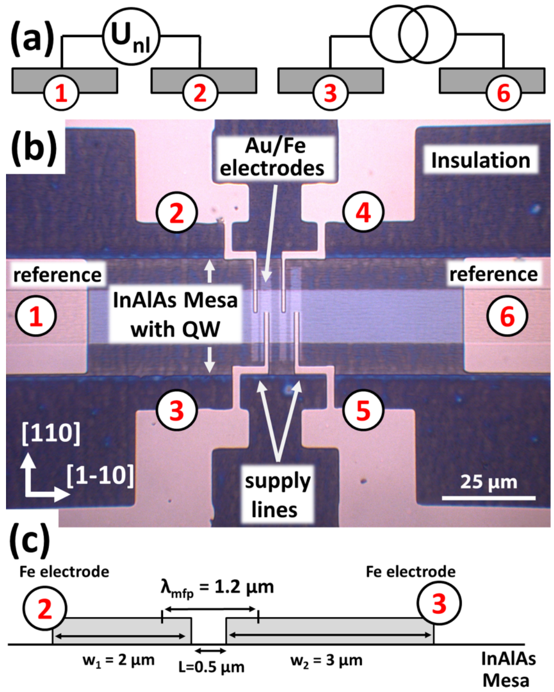

FIG. 2. (a) Circuitry of the nonlocal setup. (b) Optical image showing the top view of a fabricated lateral spin-valve device. The numbering marks the electrodes. (c) Cross section through the mesa in the $[1\bar{1}0]$ direction illustrating the relation between the mean free path and the smallest electrode distance.

The exact definition of the iron electrodes was verified separately via magnetic force microscopy. The long sides of the iron electrodes are oriented in the [110] crystal direction that matches the easy axis of iron films on InAlAs [31] and fixes the crystallographic orientation of the injected carrier spin. We note that in InAs QWs, due to the combined bulk and structure inversion asymmetry, carrier momenta in the $[1\bar{1}0]$ direction are associated with an effective magnetic field oriented in the [110] direction [4,32,33] and hence aligned in parallel with the spin orientation of the injected carriers. This parallel alignment results in longer spin-relaxation times [34].

The spin-injection measurements in nonlocal geometry were conducted at liquid helium temperatures. An in-plane magnetic field B is applied along the easy axes of the iron electrodes. The field is ramped with a rate of 2.4 mT/min from negative to positive values and vice versa. As a result of the different electrode widths and thus different coercive fields, with increasing magnetic field the electrode magnetizations switch from parallel to antiparallel and back to parallel orientation. As indicated in the inset of Fig. 3, the current I is driven between electrodes No. 3 and No. 6 and the nonlocal voltage U_{nl} is recorded between electrodes No. 2 and No. 1. Clear characteristic jumps ΔU_{nl} are observed in U_{nl} when the relative orientation of the electrode magnetization switches from parallel to antiparallel and vice versa. The jumps ΔU_{nl} reflect the imbalance of spin-up and spin-down carriers in the QW [29] and are widely seen as evidence of spin injection [2,9,10,30]. A typical signal is presented in Fig. 3. We note that

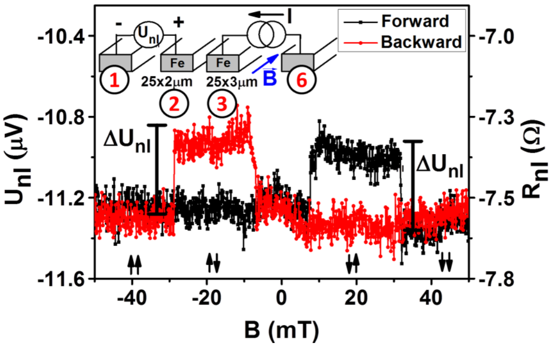

FIG. 3. The nonlocal voltage U_{nl} and $R_{\mathrm{nl}} = U_{\mathrm{nl}}/I$ vs in-plane magnetic field B at forward bias $I = +1.49\ \mu\mathrm{A}$. The experiment was conducted at liquid helium temperatures. The inset and the numbering sketch the setup and the corresponding electrodes. The arrows at the bottom indicate the relative electrodes' magnetization orientations.

ΔU_{nl} does not change sign upon current reversal, as similarly observed on Fe/GaAs structures [30], but not expected from the standard diffusive model. The assignment of spin injection is corroborated by nonlocal Hanle measurements. We observe a characteristic dip around zero perpendicular magnetic fields due to spin dephasing (measurements not shown here). Further measurements were conducted using the injector-detector electrode spacings of 1 μm (electrodes No. 3 and No. 4) and 2 μm (electrodes No. 4 and No. 5) on the same device. At these spacings no clear spin-related detector voltage jumps were observed. We note that a postgrowth, low-temperature annealing at 200 °C under nitrogen atmosphere did not lead to a further improvement of the signal, as previously observed on Fe/GaAs interfaces [35]. In contrast, a decrease of ρ_c by two orders of magnitude and no spin injection are observed after annealing. We attribute the drastic decrease of ρ_c to an interdiffusion of iron atoms into the InAlAs cover layer.

The nonlocal resistance $\Delta R_{\mathrm{nl}} = \Delta U_{\mathrm{nl}}/I$ is calculated from ΔU_{nl}. In our measurements we observed a maximal value of $\Delta R_{\mathrm{nl}} = 0.47\ \Omega$. In the purely diffusive regime the nonlocal resistance is described by [2,12,36]

$$\Delta R_{\mathrm{nl}} = \frac{\eta_{\mathrm{inj}}\eta_{\mathrm{det}}\rho_{\mathrm{sc}}\lambda_{\mathrm{diff}}}{w} e^{-\frac{L}{\lambda_{\mathrm{diff}}}}. \tag{2}$$

Here, L and w are the electrode center-to-center distance and the mesa width, respectively. Assuming that in the low-bias regime the spin-injection efficiencies at the injector η_{inj} and at the detector η_{det} are equal, Eq. (2) yields a spin-injection efficiency η of about 77%. Here, we used reported values for the spin-diffusion length $\lambda_{\mathrm{diff}} = 1.5\ \mu$m [10,12] in similar heterostructures, an electrode center-to-center distance of $L = 3\ \mu$m, and a channel resistivity of $\rho_{\mathrm{sc}} = 116\ \Omega/\square$. This spin-injection efficiency value is very large compared to previous reports on similar systems, but with a larger contact separation, i.e., in the diffusive limit. The largest value found in those reports is 8%, obtained with a device containing MgO tunneling barriers [10,12]. In correspondence to the previous report by Oltscher *et al.* [2] on GaAs spin-valve devices, we associate our large spin-efficiency result to the fact that it was obtained with a diffusive model, whereas the device is at least partly ballistic. Applying the standard diffusive model, Oltscher *et al.* calculated spin-injection efficiencies that are even unphysically large, i.e., above 100%.

Recently, an extension of the diffusive spin-injection model was proposed by Chen *et al.* [3], taking into account ballistic transport. In this model, ΔR_{nl} is given by [3]

$$\Delta R_{\mathrm{nl}} = \left(1 + \frac{\lambda_{\mathrm{mfp}}^2}{\lambda^2}\right)\frac{\eta_{\mathrm{inj}}\eta_{\mathrm{det}}\rho_{\mathrm{sc}}\lambda}{w} e^{-L/\lambda}, \tag{3}$$

$$\lambda = \frac{\hbar^2}{2m^*\alpha}, \tag{4}$$

where λ is the ballistic spin-dephasing length. Importantly, in the purely ballistic case, λ fundamentally differs from λ_{diff}. It only depends on the inverse strength of the SOI, i.e., a strong SOI necessarily leads to short λ. Using the experimentally determined value $\alpha = 4 \times 10^{-12}$ eV m in the QWs under study and $m^* = 0.036 m_e$ [24] yields $\lambda = 0.25\ \mu$m. We note that λ calculated from α in similar heterostructure designs [9,12,24,26] yields even shorter values.

Applying Eq. (3), the spin-injection efficiency was estimated considering two electrode distances L: the injector-detector edge-to-edge distance of 500 nm, which marks a lower limit, and the injector-detector center-to-center distance of 3 μm, which marks an upper limit. With the edge-to-edge distance $L = 500$ nm and the center-to-center distance 3 μm, spin-injection efficiencies of 39% and 5700% are obtained, respectively. We consider these spin-injection efficiencies to be unphysically large and suspect that the origin of those values is the assumed magnitude of the ballistic spin-dephasing length λ. The inverse proportionality between λ and α indicates that the SOI always destabilizes the carrier spin, leading to short spin-dephasing lengths. However, in the crystallographic orientation of our spin-valve devices the spins are expected to be stabilized by spin-orbit coupling [4,32–34], which should result in a larger spin-dephasing length [4,32–34]. Considering the anisotropy of the SOI in our heterostructures, Eq. (3) predicts lower spin-injection efficiencies. Therefore, we suppose the spin-dephasing length in the crystallographic orientation of our spin-valve devices to be larger. A first indication of a larger value for λ is given by the evaluation of the Hanle data with a diffusive model [30], yielding $\lambda_{\mathrm{H}} = 0.73\ \mu$m. Although knowing that the diffusive Hanle model does not apply in the intermediate regime, the larger value of λ_{H} compared to λ indicates λ might be larger.

In conclusion, we have demonstrated spin injection into InGaAs/InAs QWs using lateral spin-valve devices and a nonlocal setup. The spin valves are designed such that the transport can be assumed to be at least partly ballistic. Nonetheless, applying the standard diffusive model yields an extremely large spin-injection efficiency of about 77%, similar to a previous report [2] on spin-valve devices with a small SOI material. For the evaluation of our data we apply a recent ballistic model proposed for the ballistic limit. This model and our data obtained very large spin-injection efficiencies, suggesting that the spin-dephasing length introduced in the model is too small to explain our data. We infer that in the devices under study it is crucial to consider the crystal orientation dependence of the SOI.

We gratefully acknowledge helpful discussions with K. Vyborny and M. Stier. This work is financially supported from the Deutsche Forschungsgemeinschaft via Graduiertenkolleg No. 1286 and the Bundesministerium für Bildung und Forschung via Project No. 01DS16022.

[1] H. Jaffrès, Physics **7**, 123 (2014).
[2] M. Oltscher, M. Ciorga, M. Utz, D. Schuh, D. Bougeard, and D. Weiss, Phys. Rev. Lett. **113**, 236602 (2014).
[3] K. Chen and S. Zhang, Phys. Rev. B **92**, 214402 (2015).
[4] A. Manchon, H. C. Koo, J. Nitta, S. M. Frolov, and R. A. Duine, Nat. Mater. **14**, 871 (2015).
[5] A. Hirohata and K. Takanashi, J. Phys. D **47**, 193001 (2014).
[6] S. Datta and B. Das, Appl. Phys. Lett. **56**, 665 (1990).
[7] M. Zwierzycki, K. Xia, P. J. Kelly, G. E. W. Bauer, and I. Turek, Phys. Status Solidi A **196**, 25 (2003).
[8] O. Wunnicke, P. Mavropoulos, R. Zeller, P. H. Dederichs, and D. Grundler, Phys. Rev. B **65**, 241306(R) (2002).
[9] H. C. Koo, J. H. Kwon, J. Eom, J. Chang, S. H. Han, and M. Johnson, Science **325**, 1515 (2009).
[10] H. C. Koo, H. Yi, J.-B. Ko, J. Chang, S.-H. Han, D. Jung, S.-G. Huh, and J. Eom, Appl. Phys. Lett. **90**, 022101 (2007).
[11] P. R. Hammar and M. Johnson, Phys. Rev. Lett. **88**, 066806 (2002).
[12] T. Ishikura, L.-K. Liefeith, Z. Cui, K. Konishi, K. Yoh, and T. Uemura, Appl. Phys. Express **7**, 073001 (2014).
[13] C. Heyn, S. Mendach, S. Löhr, S. Beyer, S. Schnüll, and W. Hansen, J. Cryst. Growth **251**, 832 (2003).
[14] A. Richter, M. Koch, T. Matsuyama, C. Heyn, and U. Merkt, Appl. Phys. Lett. **77**, 3227 (2000).
[15] S. Mendach, C. M. Hu, C. Heyn, S. Schnüll, H. P. Oepen, R. Anton, and W. Hansen, Physica E **13**, 1204 (2002).
[16] S. Lohr, S. Mendach, T. Vonau, C. Heyn, and W. Hansen, Phys. Rev. B **67**, 045309 (2003).
[17] NEXTNANO GmbH, http://www.nextnano.com/tools/nextnanomat.php.
[18] E. H. Hall, Am. J. Math. **2**, 287 (1879).
[19] L. Shubnikov and W. J. de Haas, Nature (London) **126**, 500 (1930).
[20] K. v. Klitzing, G. Dorda, and M. Pepper, Phys. Rev. Lett. **45**, 494 (1980).
[21] J. G. Simmons, J. Appl. Phys. **34**, 1793 (1963).
[22] R. Tsu, Appl. Phys. Lett. **22**, 562 (1973).
[23] U. Kunze, Z. Phys. B: Condens. Matter **76**, 463 (1989).
[24] D. Grundler, Phys. Rev. Lett. **84**, 6074 (2000).
[25] G. Engels, J. Lange, T. Schapers, and H. Luth, Phys. Rev. B **55**, R1958(R) (1997).
[26] J. Nitta, T. Akazaki, H. Takayanagi, and T. Enoki, Phys. Rev. Lett. **78**, 1335 (1997).
[27] M. Johnson and R. H. Silsbee, Phys. Rev. Lett. **55**, 1790 (1985).
[28] M. Johnson and R. H. Silsbee, Phys. Rev. B **37**, 5326 (1988).
[29] R. Silsbee, Bull. Magn. Reson. **2**, 284 (1980).
[30] X. Lou, C. Adelmann, S. A. Crooker, E. S. Garlid, J. Zhang, K. S. M. Reddy, S. D. Flexner, C. J. PalmstrØm, and P. A. Crowell, Nat. Phys. **3**, 197 (2007).
[31] N. Tournerie, P. Schieffer, B. Lepine, C. Lallaizon, P. Turban, and G. Jezequel, Phys. Rev. B **78**, 134401 (2008).
[32] R. Winkler, Phys. Rev. B **69**, 045317 (2004).
[33] R. Winkler, *Spin-Orbit Coupling Effects in Two-Dimensional Electron and Hole Systems*, Springer Tracts in Modern Physics Vol. 191 (Springer, Berlin, 2003).
[34] J. L. Cheng, M. W. Wu, and I. C. da Cunha Lima, Phys. Rev. B **75**, 205328 (2007).
[35] L.-K. Liefeith, R. Tholapi, M. Hänze, R. Hartmann, T. Slobodskyy, and W. Hansen, Appl. Phys. Lett. **108**, 212404 (2016).
[36] B. Dlubak, M.-B. Martin, C. Deranlot, B. Servet, S. Xavier, R. Mattana, M. Sprinkle, C. Berger, W. A. De Heer, F. Petroff, A. Anane, P. Seneor, and A. Fert, Nat. Phys. **8**, 557 (2012).